






## Thermal transport in warm dense matter revealed by refraction-enhanced x-ray radiography with a deep-neural-network analysis

S. Jiang <sup>1✉</sup>, O. L. Landen <sup>1</sup>, H. D. Whitley<sup>1</sup>, S. Hamel <sup>1</sup>, R. London<sup>1</sup>, D. S. Clark<sup>1</sup>, P. Sterne<sup>1</sup>, S. B. Hansen<sup>2</sup>, S. X. Hu <sup>3</sup>, G. W. Collins<sup>3</sup> & Y. Ping <sup>1</sup>

Transport properties of high energy density matter affect the evolution of many systems, ranging from the geodynamo in the Earth's core, to hydrodynamic instability growth in inertial confinement fusion capsules. Large uncertainties of these properties are present in the warm dense matter regime where both plasma models and condensed matter models become invalid. To overcome this limit, we devise an experimental platform based on x-ray differential heating and time-resolved refraction-enhanced radiography coupled to a deep neural network. We retrieve the first measurement of thermal conductivity of CH and Be in the warm dense matter regime and compare our measurement with the most commonly adopted models. The discrepancies observed are related to the estimation of a correction term from electron-electron collisions. The results necessitate improvement of transport models in the warm dense matter regime and could impact the understanding of the implosion performance for inertial confinement fusion.

<sup>1</sup>Lawrence Livermore National Laboratory, Livermore, CA, USA. <sup>2</sup>Sandia National Laboratory, Albuquerque, NM, USA. <sup>3</sup>Laboratory for Laser Energetics, Rochester, NY, USA. ✉email: [jiang8@llnl.gov](mailto:jiang8@llnl.gov)

Warm dense matter (WDM) physics has been identified as a challenging research area in high-energy-density physics<sup>1</sup>. The challenges lie in both theoretical modeling and experimental measurements. Due to its unique location in the density-temperature map at the junction of plasma, solid and liquid states, many of the assumptions and approximations that have been successfully applied either in plasma physics or in condensed matter theory, such as the adiabatic assumption between electrons and ions, statistical equilibrium treatments of electron temperature, and negligible potential energy compared to kinetic energy (or vice versa), do not apply, making it difficult to develop a consistent model for WDM. On the other hand, the high-energy-density nature results in fast-evolving states and transient phenomena, making experimental study also challenging. This has left WDM a largely uncharted frontier. Nonetheless, WDM has been drawing increasing attention, driven by its central role in bridging the gap between condensed matter and plasma physics. The properties of WDM are important for the success of ICF experiments, and understanding them will significantly extend the limits of knowledge in plasma physics as well as in other areas, such as astrophysics, planetary physics, geophysics, and material science.

The thermal conductivity in the WDM regime is of particular interest as it can impact the growth of hydro-instabilities at the ablator-fuel interface of the imploding ICF capsule<sup>2</sup>. During the implosion around peak velocity, the ablator-fuel interface reaches  $\sim 10$  g/cc and  $\sim 20$ – $30$  eV in the ablator versus  $< 10$  eV in the DT fuel. Rayleigh–Taylor instabilities that occur at the interface can lead to the mixing of ablator material into the fuel, and if severe enough, in the central hot spot it can substantially reduce the implosion confinement and fusion yield. Thermal conduction across the temperature gradient at the interface leads to a predicted development of a density gradient near the interface, which can stabilize high-mode instabilities with wavelengths shorter than the scale length. Therefore knowing the thermal conductivity is critical for the correct prediction of the mix width. Besides the impact on ICF ignition, conductivity also plays an essential role in many other energy transport processes, such as MeV electron transport for fast ignition, generation of magnetic fields, and the formation of return current for resistive heating in WDM.

Despite the importance of conductivity in WDM, a scarcity of experimental data in the relevant regime has left all models unverified. Such experiments require creation, careful characterization, and correct measurements of WDM. In this paper, we present measurements using an experimental platform based on x-ray differential heating<sup>3</sup> and phase contrast imaging. The concept of the experiment is illustrated in Fig. 1. First, the target is isochorically heated by judicious choice of x-rays energy such that lower-density CH absorbs more than Be due to their different opacities. As a result, a temperature jump is induced initially between CH and Be. The subsequent thermal conduction leads to the development of a temperature gradient at the interface. Rapid pressure balance across the interface drives the density to compensate the temperature slope, and the density profile change is measured by refraction-enhanced radiography. Higher conductivity will result in a longer density gradient, and less contrast in the radiograph. Therefore thermal conductivity can be determined from the evolution of the density gradient near the interface.

## Results

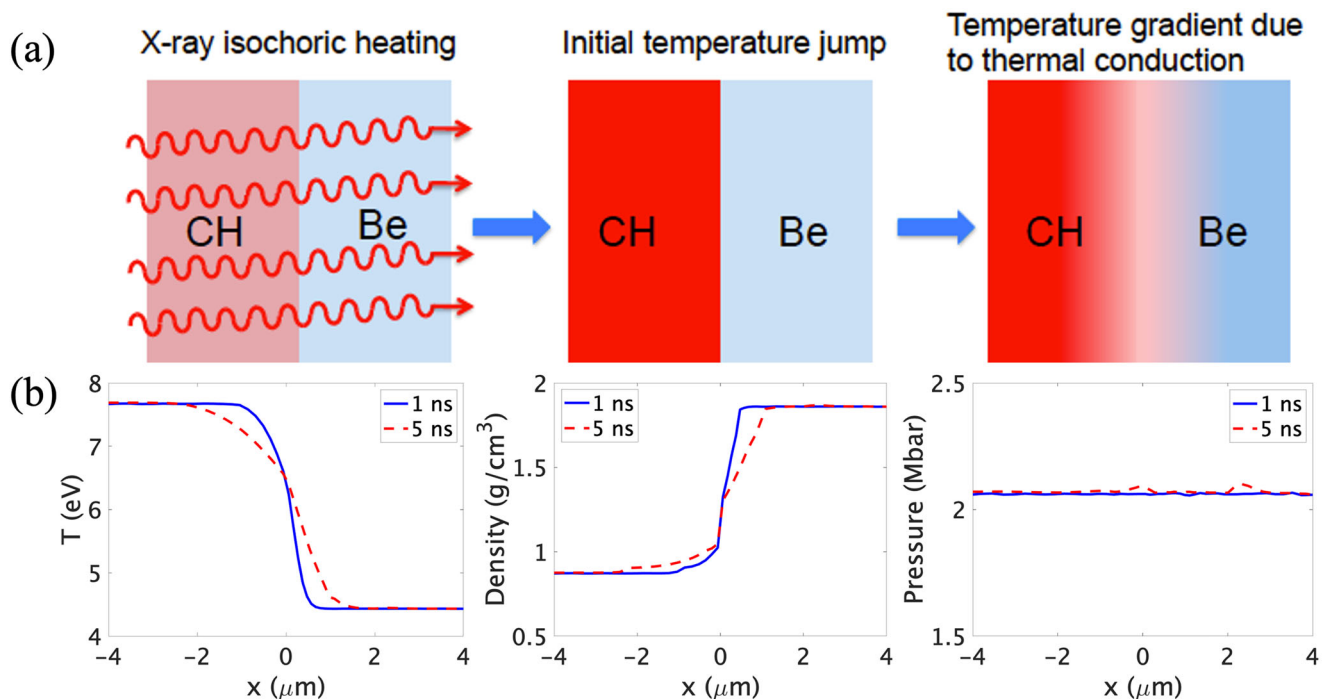
The experiments were performed on the OMEGA laser at Laboratory for Laser Energetics (LLE) at the University of Rochester. The experiment is illustrated in Fig. 2a. The experimental configuration was similar to that of a previous experiment<sup>4</sup> with a vanadium backlighter and a CH/Be target

containing a cylindrical interface with a radius of curvature of 1.0 mm. The CH/Be target was heated by x-rays from both sides: one side with Ag L-band emission around 3.5 keV generated by a silver foil attached to the Be side, the other side with Sn L-band around 4 keV. Each side was irradiated by 14 laser beams (1 ns flat-top pulse shape and total energy of 7 kJ). The X-rays heat lower-density CH to a higher temperature since it has a higher absorption coefficient per atom than Be. The radius of the curved interface was chosen for easy alignment, contrast enhancement<sup>5</sup>, and quasi-1D geometry. The thicknesses of the Be, 500  $\mu\text{m}$  at one side and 300  $\mu\text{m}$  at the other side, were chosen to delay the laser-generated shocks reaching the interfaces and to isolate the CH/Be interfaces from the laser-plasma interaction (LPI) regions. The vanadium backlighter foil was irradiated by ten beams with 1 ns flat-top pulse shape and total energy of 5 kJ. A  $\sim 5$   $\mu\text{m}$  slit in front of the V foil created an effective line source for the radiography. The backlighter X-rays were bent due to refraction at the CH/Be interface, forming bright and dark fringes in the radiograph. Because the conduction-induced density gradient only exists within a few microns from the interface, a large magnification ( $\sim 60$ ) was necessary to resolve the fine features. The radiographs were recorded by an X-ray framing camera (XRFC) with a gate pulse of 200 ps. The delay between the backlighter beams and the heater beams was varied to probe the evolution of the interface.

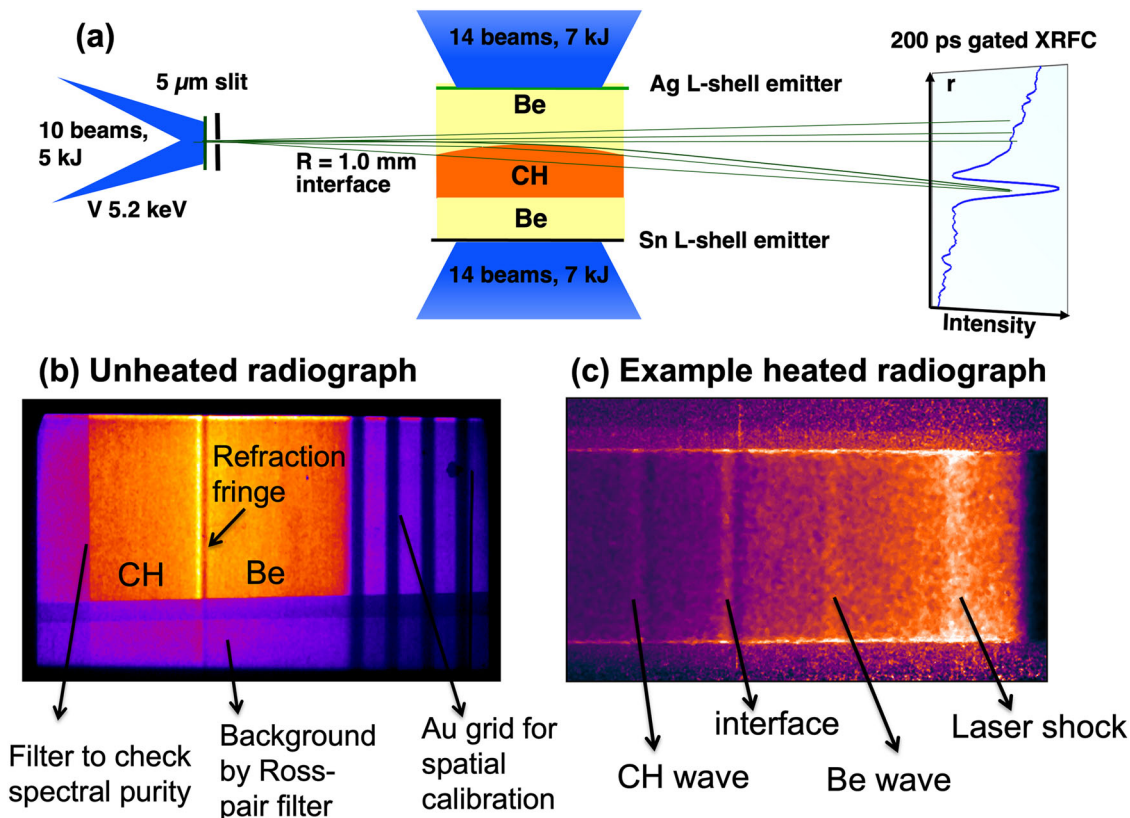
An unheated radiograph is displayed in Fig. 2b, showing the gold grid at the right for spatial calibration, a Mylar strip at the left edge for checking backlighter spectral purity, and the background obtained by differential filtering through a V/Ti Ross-pair filter on the bottom. The transmission of the Mylar strip is 41–48% after background subtraction, corresponding to an x-ray energy range of 5.2–5.5 keV. This is consistent with Vanadium line emissions at 5.2 keV ( $He_{\alpha}$ ) and 5.4 keV ( $Ly_{\alpha}$ ). Ray-tracing results at 5.2 and 5.5 keV for our CH/Be targets show that the difference is much less than the noise level. This x-ray energy is also well above any absorption edges in CH and Be so that the refractive index is a function of the total electron density<sup>6</sup>. The unheated radiograph shows a clear refractive fringe corresponding to the interface. The contrast mainly depends on the backlighter source size, set by the 5- $\mu\text{m}$  slit, and the CH/Be target surface quality and provides a baseline for data analysis. The root mean square surface roughness of the CH/Be interface has been measured by scanning electron microscopy to be 0.23  $\mu\text{m}$ <sup>4</sup>. Therefore the 5- $\mu\text{m}$  source size is the major factor determining the contrast of the unheated fringe. The source function can be accurately obtained from the Au grid image (see Instrument function in Methods). Besides the unheated data, a flatfield of the XRFC was also taken to provide the correct normalization of the radiographs.

Figure 2c shows an example of a heated radiograph. Three fringes show up in the image, the middle one representing the interface, and two side ones corresponding to the waves propagating in CH and Be, respectively. A shock wave driven by the laser, traveling from right to left, is also visible. The thicknesses of the Be layers have been chosen to delay the laser-driven shocks to allow for thermal conduction to occur at the interface while being still transmissive for heating X-rays. Radiographs up to 6.8 ns are recorded before the laser shock interferes with the interface.

The radiograph lineouts at six delays are plotted in the left column in Fig. 3, revealing the interesting evolution of the CH/Be interface. The first row at 0 ns corresponds to the unheated target, providing a baseline for the interface before heating. The x-ray heating induced an initial temperature jump between CH and Be, which resulted in an initial pressure jump, creating weak compression and rarefaction waves propagating away from the interface. The high sensitivity of the refraction-enhanced radiography to discontinuities has enabled observation of these waves<sup>7</sup>. From the intensity lineouts at early time 2.1 and 2.8 ns in Fig. 3, we can clearly see waves forming and



**Fig. 1 Methodology for measuring thermal conductivity.** **a** Three sequential events in the experiment. **b** Profiles of temperature, density, and pressure across the interface once a gradient is developed by conduction, showing that the density profile compensates the temperature slope to balance the pressure (from 1D HYADES<sup>30</sup> simulations).



**Fig. 2 Schematic of the experimental setup.** **a** Experimental schematic. The thickness of the layers was 500 μm Be, 200 μm CH, and 300 μm Be, respectively, to allow heating from both sides. The length of the target is 3 mm. **b** A radiograph of an undriven target, showing the gold grid for spatial calibration, a Mylar strip at the left edge for checking backlighter spectral purity, and the background obtained by a V/Ti Ross-pair filter. **c** An example radiograph of the heated CH/Be target.

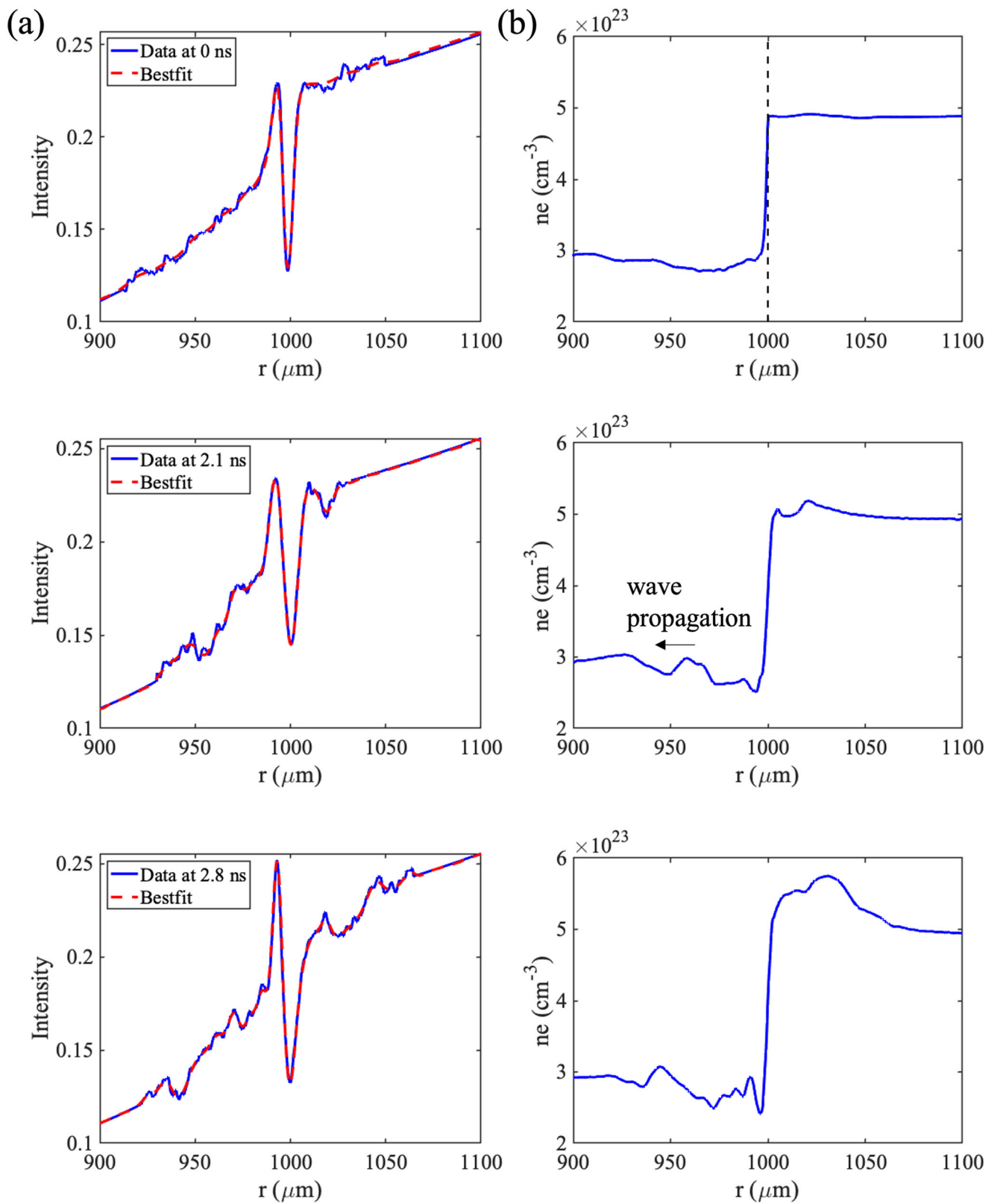


**Fig. 3** The density profiles retrieved from the measured refraction-enhanced radiograph (RER) intensities using a deep neural network. **a** Shows the RER intensity lineouts and **b** Shows the retrieved density profiles. The red dashed curves are calculated intensity lineouts from the densities. The CH/Be interface is located at  $r = 1000 \mu\text{m}$ . The corresponding time delays are labeled as unheated, 2.1, 2.8, 4.1, 6.1, and 6.8 ns.

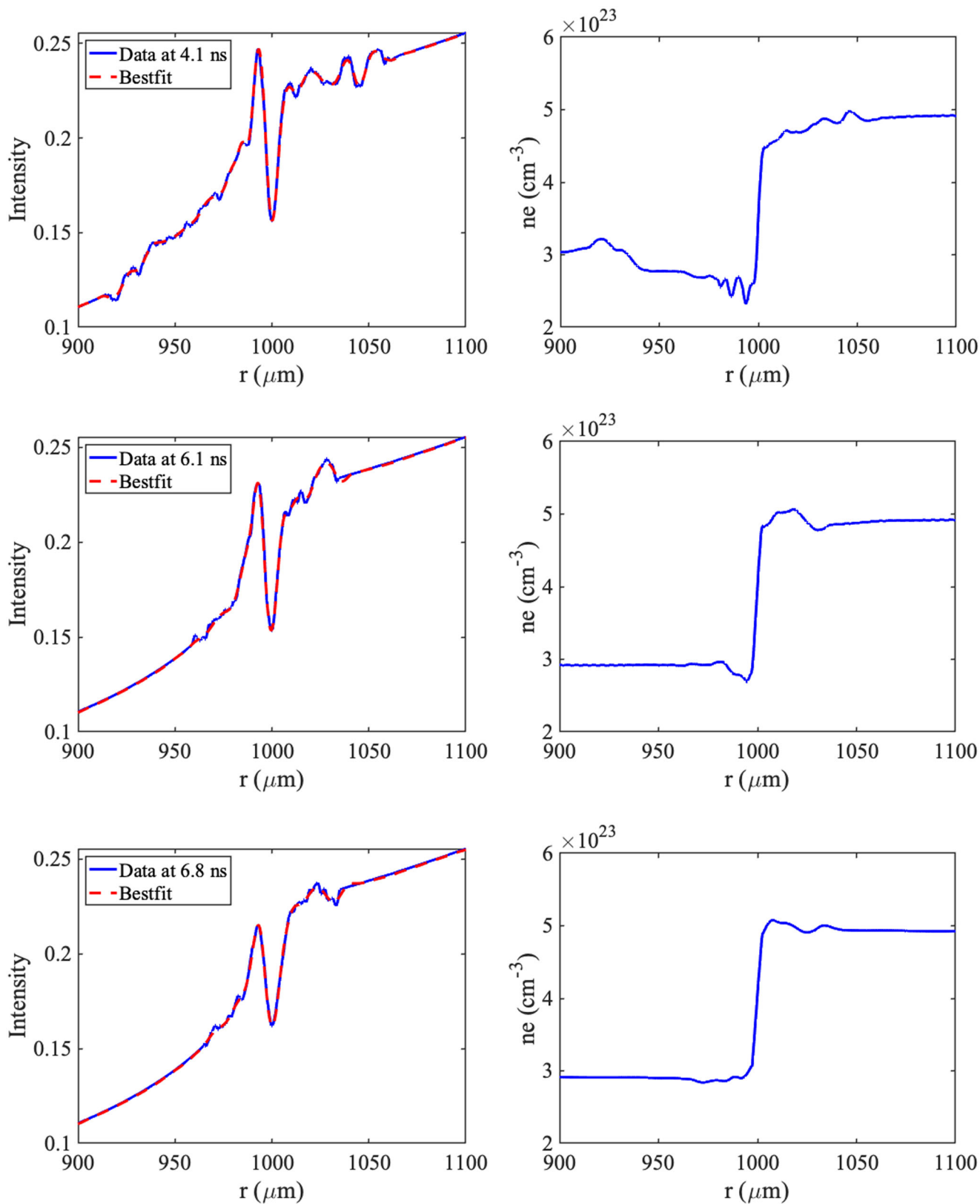
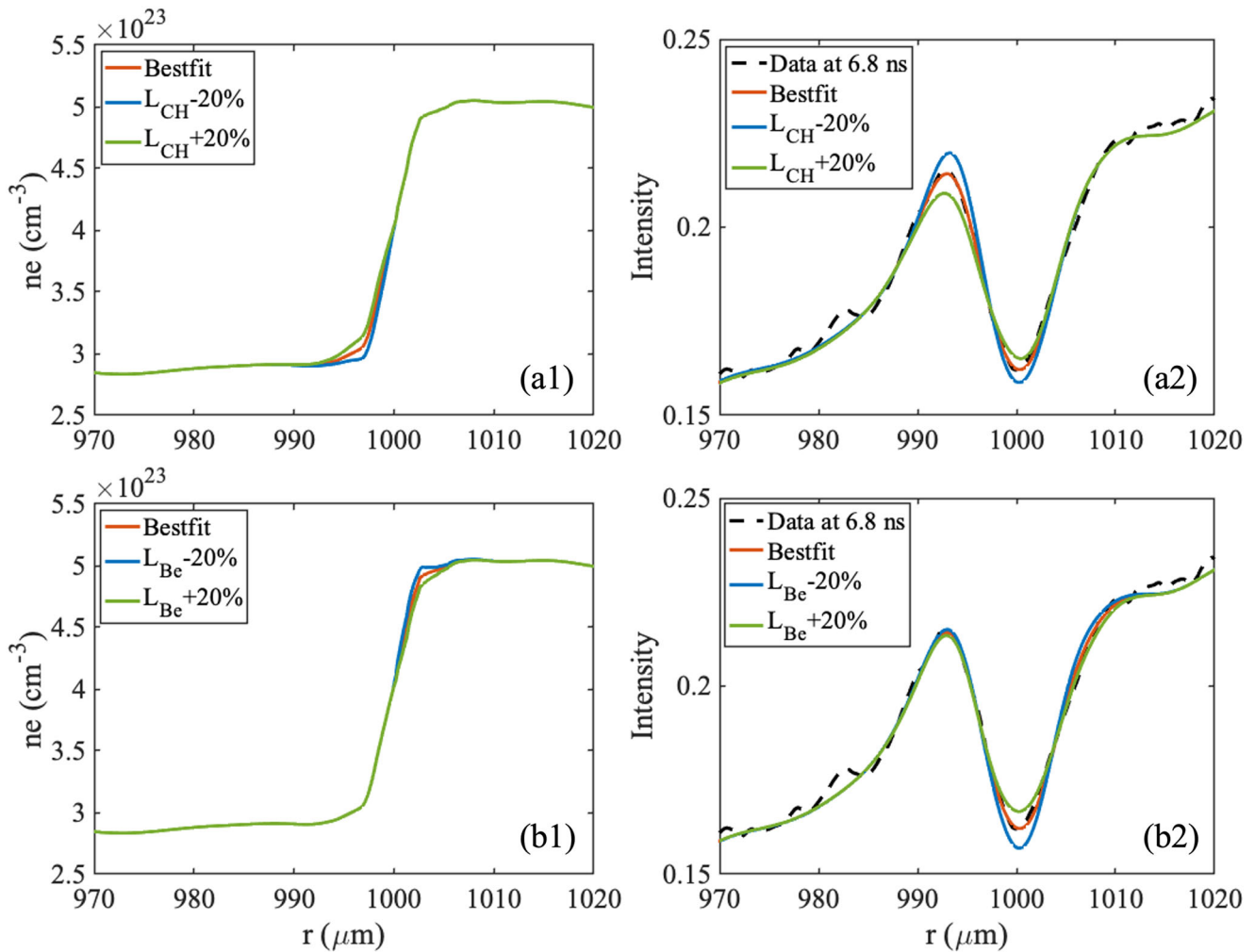


Fig. 3 Continue



**Fig. 4 Sensitivity of the data fits the scale length of CH and Be.** a1, b1 Shows the density profiles when we change the scalelengths on the CH and the Be side correspondingly. The curves in (a2, b2) are intensity lineouts from data (black dashed lines), best fit (red solid lines), shorter scale lengths (blue solid lines), and longer scale lengths (green solid lines). The variation is  $\pm 20\%$  in  $L_{CH}$  and  $L_{Be}$ .

propagating. At a later time, the waves have propagated farther away and decayed, and a density gradient across the interface is created to compensate for thermal conduction. The density scale length at the interface increases so that the fringe contrast at the interface decreases as expected.

We use a deep neural network analysis to reconstruct the detailed density profiles at these time delays (see Density retrieval in Methods). The right column in Fig. 3 shows the retrieved profiles of total electron density  $n_e$ . The red dashed curves in the left column are calculated intensity lineouts from the reconstructed densities. The good agreement with the measured lineouts confirms the validity of our density retrieval process. We first quantify the density scale lengths in both CH and Be at times after 4 ns when the waves have propagated away from the interface so that the density gradient evolution is dominated by thermal conduction. The density profiles near the interface in the range of 980–1020  $\mu\text{m}$  are fit by two Fermi-like functions to define the density scale lengths in CH and Be,  $L_{CH}$ , and  $L_{Be}$ , respectively.

$$n_e(r) = \begin{cases} \frac{n_{e1a}}{e^{-(r-r_0)/L_{CH}} + 1} + n_{e2a}, & \text{for } r < r_0 \\ \frac{n_{e1b}}{e^{-(r-r_0)/L_{Be}} + 1} + n_{e2b}, & \text{for } r \geq r_0 \end{cases} \quad (1)$$

Here  $r_0$  is the radius of the interface. Two independent Fermi functions were used to fit the CH side ( $r < r_0$ ) and the Be side

( $r > r_0$ ) separately, while keeping  $n_e$  continuous at  $r = r_0$ . Parameters  $n_{e1a}$ ,  $n_{e2a}$ ,  $L_{CH}$ ,  $n_{e1b}$ ,  $n_{e2b}$ , and  $L_{Be}$  were all determined by the Fermi fitting.  $L_{CH}$  and  $L_{Be}$ , therefore, stands for the fitting scalelengths for the electron densities on the CH and Be sides correspondingly. At 6.8 ns for example,  $L_{CH} = 1.3 \mu\text{m}$  and  $L_{Be} = 1.1 \mu\text{m}$ . In order to test the sensitivity of the measured RER lineout to the scale lengths, we vary these scale lengths while maintaining the detailed features of the density profile, as is shown in Fig. 4. As the CH scale length varies, both amplitudes of the peak and the valley in the radiograph lineout change. On the other hand,  $L_{Be}$  mainly affects the valley amplitude. The scale length uncertainties are about 20%, determined as when the variation in the amplitude is comparable to the noise level.

The next step is to determine the heated temperatures in both CH and Be. We did not have direct temperature diagnostics but found that the sound speed is sensitive to the bulk temperature under the conditions of our experiments. The sound speed in CH is measured from the propagating waves at early time delays. Figure 5a shows the reconstructed density profiles at 2.1 and 2.8 ns to highlight the wave propagation in CH. The wavelets at these two delays overlap reasonably well if we shift the profile at 2.1 ns by  $-14 \pm 0.8 \mu\text{m}$  as shown in the inset, indicating a sound speed of  $20 \pm 1 \mu\text{m/ns}$  in CH. This speed also matches the location of the wave at 2.1 ns compared to the interface. The CH temperature as a function of sound speed from various CH

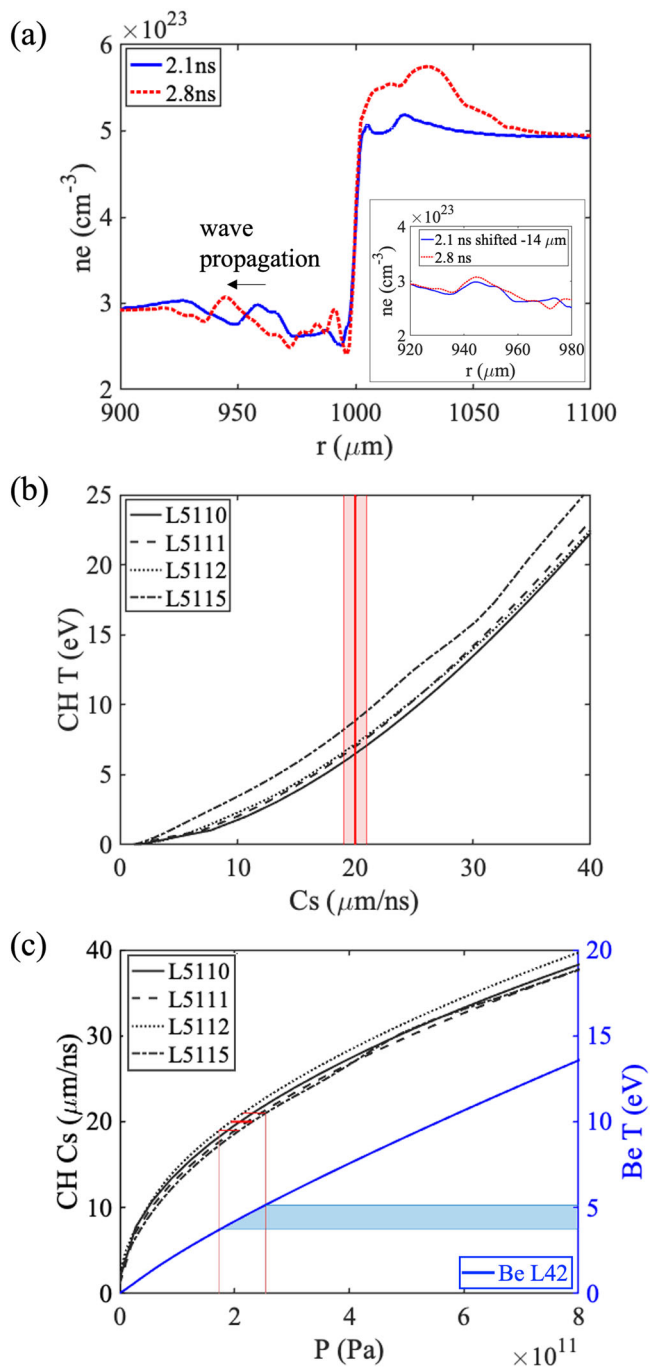


**Fig. 5 Determine the temperature from the sound speed measurement.** **a** Electron density profile at 2.8 ns (blue curve) and 2.1 ns (red dashed curve) for measuring the sound speed in CH. The inset shows the 2.1 ns wave profile at the CH side shifted by  $-14 \mu\text{m}$  matches the 2.8 ns profile. **b** Black curves: temperature as a function of sound speed for CH from various EOS tables. Red line and shaded area: the measured sound speed with error bars. **c** Left y-axis: sound speed as a function of pressure for CH from various EOS tables. The horizontal red lines indicate the measured sound speed. The vertical red lines show the determined pressure range. Right y-axis: temperature as a function of pressure for Be from the L42 EOS table. The blue shaded area is the temperature range in Be when CH and Be reaches a pressure balance.

equation of state (EOS) tables<sup>8,9</sup> is plotted in Fig. 5b. The curves are at a constant density of  $0.9 \text{ g/cm}^3$ , which is measured from the unheated radiograph. These differences between these curves are taken as the uncertainty in the T–Cs relationship. The vertical

red bars indicate the range in the measured CH wave velocity. By comparing it with the EOS curves the temperature for CH is determined to be  $7.8 \pm 1.8 \text{ eV}$ . On the Be side of the interface, the wave propagation is not as well defined as in CH. Therefore we need to use other observables to constrain the temperature in Be.

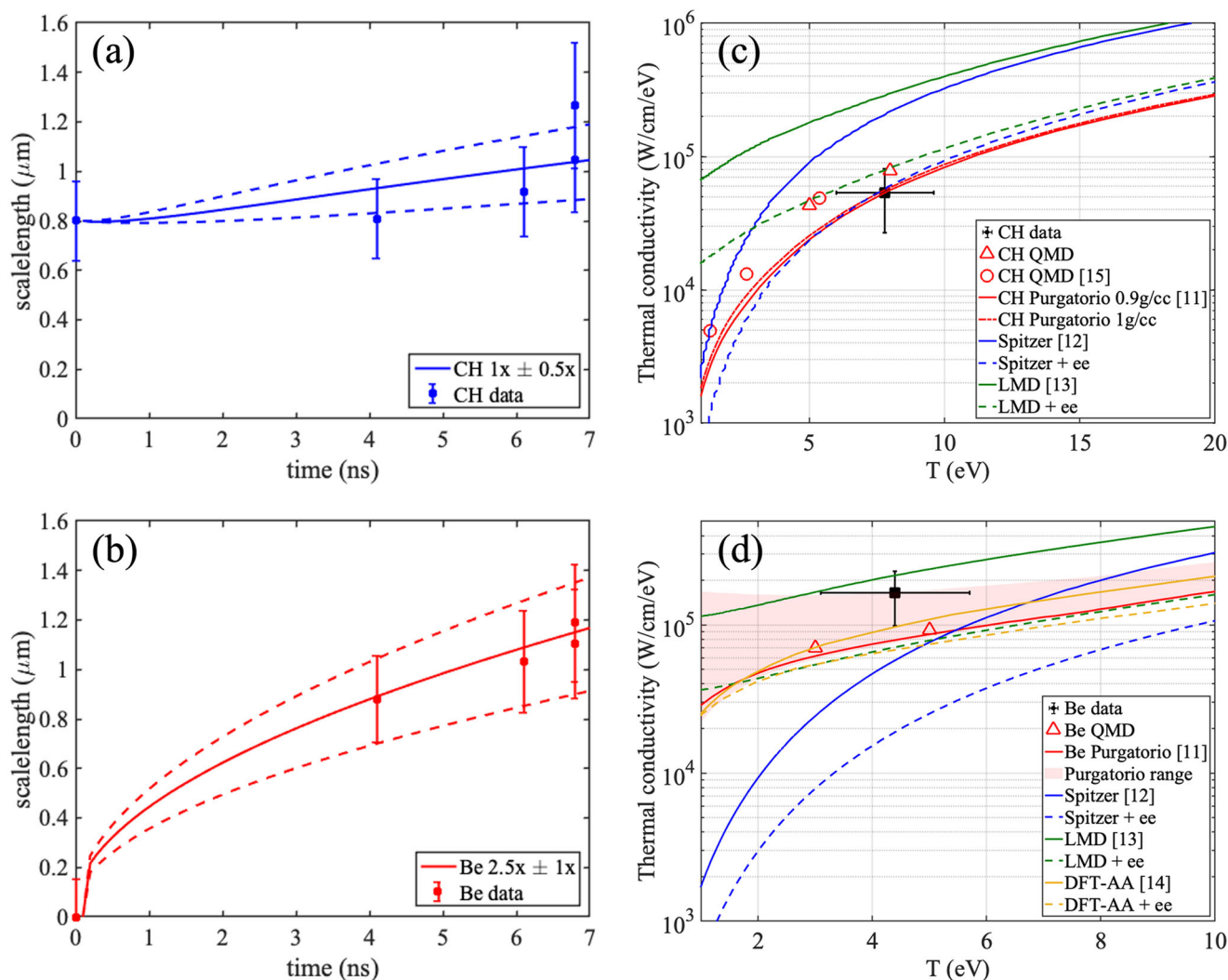
It is apparent in Fig. 5a that the interface did not move within our experimental precision, which indicates a pressure balance between CH and Be during this time. These two radiographs were taken in the same shot using a two-strip framing camera so that there is no ambiguity in the alignment between these two density profiles. This pressure equilibration between CH and Be is utilized to determine the temperature in Be. Figure 5c shows the CH sound speed vs pressure (left y-axis) and Be temperature vs pressure (right y-axis) at the measured mass densities of  $0.9 \text{ g/cm}^3$  in CH and  $1.84 \text{ g/cm}^3$  in Be. A recent EOS table L42 based on QMD simulations was used for Be<sup>10</sup>. The measured CH sound speed corresponds to a pressure of  $214 \pm 40 \text{ GPa}$ . According to pressure balance, the Be temperature is determined to be  $4.4 \pm 0.7 \text{ eV}$ , which is shown as the blue shaded area in Fig. 5c.

To infer the thermal conductivity from the measured density scale lengths, we numerically solve the thermal conduction equations:

$$\begin{aligned} \rho_{CH} C_{CH} \frac{\partial T_{CH}}{\partial t} &= \frac{\partial}{\partial x} \kappa_{CH} \frac{\partial T_{CH}}{\partial x} \\ \rho_{Be} C_{Be} \frac{\partial T_{Be}}{\partial t} &= \frac{\partial}{\partial x} \kappa_{Be} \frac{\partial T_{Be}}{\partial x} \end{aligned} \quad (2)$$

where  $\rho$  is the mass density,  $C$  is the ideal gas heat capacity at constant pressure, and  $\kappa$  is the thermal conductivity which is from Purgatorio thermal conductivity tables<sup>11,12</sup>. The initial conditions for numerically solving the conduction equations are  $T_{CH}(t=0) = 7.8 \text{ eV}$  and  $T_{Be}(t=0) = 4.4 \text{ eV}$ . The boundary conditions are  $T_{CH}(x < 0) = 7.8 \text{ eV}$ ,  $T_{Be}(x > 0) = 4.4 \text{ eV}$ ,  $\rho_{CH}(x < 0) = 0.9 \text{ g/cc}$  (ambient density of CH),  $\rho_{Be}(x > 0) = 1.84 \text{ g/cc}$  (ambient density of Be), and thermal flux conservation  $\kappa_{CH} \frac{dT_{CH}}{dx}(x=0) = \kappa_{Be} \frac{dT_{Be}}{dx}(x=0)$ . The numerical solution has been verified by comparing with the analytical solution in the case of constant  $\rho$ ,  $C$ , and  $\kappa^3$ . We found that the calculated density profile can be fit well with a Fermi-like function with two scale lengths  $L_{CH}$  in CH and  $L_{Be}$  in Be, respectively, similar to the fit to the extracted electron density profiles. The unheated data ( $t=0$ ) in Fig. 3 indicates an initial Fermi scale length of  $0.8 \mu\text{m}$  in CH, and a scale length in Be that is smaller than  $0.15 \mu\text{m}$ . During the target fabrication, the Be tube was precisely machined, while the CH part was formed by filling the Be tube with melted CH. Therefore a smaller slope at the CH interface was expected. These scale lengths are also set as the initial conditions for the numerical calculation.

Both the measured and calculated scale lengths  $L_{CH}$  and  $L_{Be}$  as a function of time are shown in Fig. 6a, b. During the experiment, we have repeated the shot at 6.8 ns to check the reproducibility. As the interface is differentially heated, both the  $L_{CH}$  and the  $L_{Be}$  increases to  $\sim 1.1 \mu\text{m}$  at 6.8 ns. The calculated scale lengths using the conduction equations with Purgatorio thermal conductivity tables are  $\approx 1.1 \mu\text{m}$  for CH but only  $\approx 0.7 \mu\text{m}$  for Be at 6.8 ns. The faster growth in the Be scale length indicates a larger thermal conductivity than the prediction from Purgatorio. Multipliers in the CH and Be thermal conductivity were applied to match the measured time history of the scale lengths, which is found to be about  $1 \times$  for CH and  $2.5 \times$  for Be, shown as the solid lines in Fig. 6a, b. The dashed lines are variations of the multipliers, which is  $1 \pm 0.5 \times$  for CH and  $2.5 \pm 1 \times$  for Be. This range generally matches the uncertainty in the data. We have also tested the results with the Dulong–Petit heat capacity and the change in the fitted thermal conductivity is well within this error bar. However, the specific heat capacity is still model-dependent and can be different if other models are applied. This effect deserves further investigation.



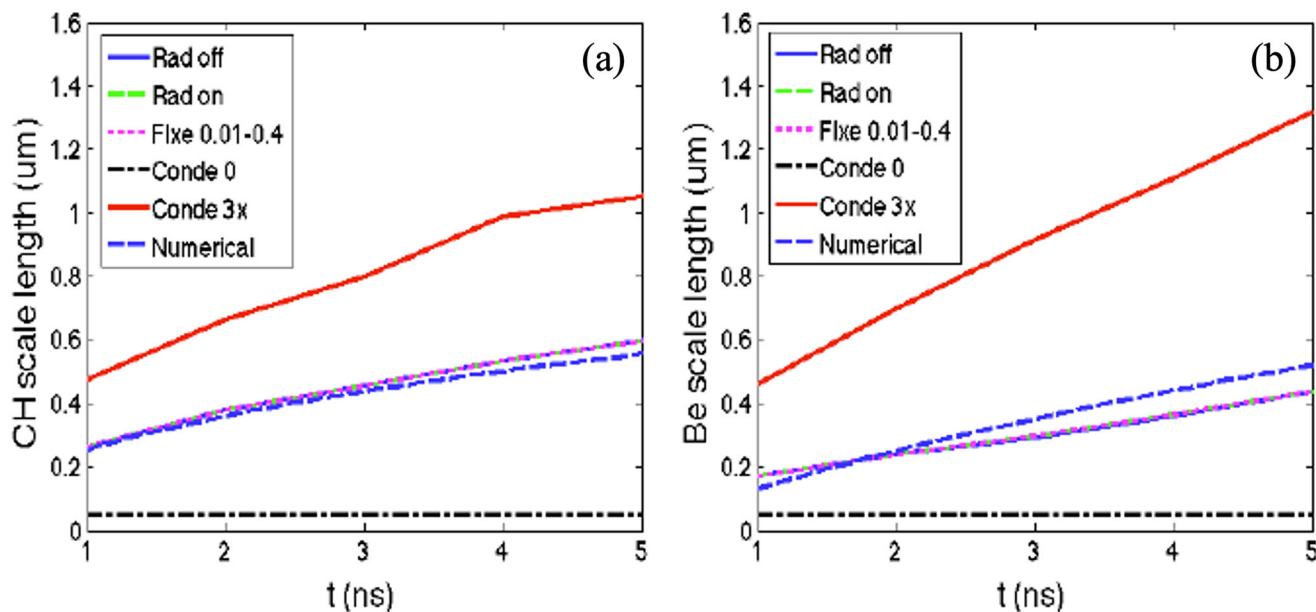
**Fig. 6 Thermal conductivities for CH and Be.** Best-fit CH (a) and Be (b) scale lengths vs time. Also shown are calculated scale lengths using the conduction equations with a multiplier of  $1 \times$  for CH and  $2.5 \times$  for Be (solid lines), and varying the CH multiplier by  $\pm 0.5 \times$  and the Be multiplier by  $\pm 1 \times$  (dashed lines). **c, d** Comparison between the thermal conductivity inferred from the data and various models. The horizontal error bars are the temperature uncertainties shown in Fig. 5. The vertical error bars are the uncertainties in thermal conductivities shown in (a) and (b).

Figure 6c, d shows the comparison between the thermal conductivity inferred from the data and various models for CH and Be, including Purgatorio<sup>11,12</sup>, Spitzer<sup>13</sup>, Lee–More–Desjarlais (LMD)<sup>14,15</sup>, density functional average-atom theory (DFT-AA)<sup>16</sup>, and QMD (quantum molecular dynamics simulations based on density functional theory DFT). The thermal conductivities derived from the experiment is  $5.4 \pm 2.7 \times 10^4 \text{ W/cm/eV}$  for CH at  $7.8 \pm 1.8 \text{ eV}$ , and  $16.4 \pm 6.6 \times 10^4 \text{ W/cm/eV}$  for Be at  $4.4 \pm 0.7 \text{ eV}$ . The details of the QMD calculations are explained in the DFT-MD Simulations in Methods. For CH we have also included the QMD calculation from ref. 17, which agrees well with our QMD simulation. For the Spitzer, LMD and DFT-AA models, we have performed calculations both with and without the correction from electron-electron collisions, which is estimated with a commonly used model from ref. 18. A reduction factor of about 0.3 – 0.7 in the calculated thermal conductivity has been found with electron-electron collisions. The results with and without the electron-electron collision effect represent the high and low bounds of model predictions. The Purgatorio tables have included the electron-electron collision by default. The details of the calculation are described in refs. 11,12. The QMD models were performed without this electron-electron collision term. Different models for

CH were performed at slightly different densities ranging from 0.9 to  $1 \text{ g/cm}^3$ . We have confirmed that this density difference caused a negligible change in thermal conductivity with the Purgatorio model. For Be, the Spitzer and LMD models were performed at the same density as the experiment ( $1.84 \text{ g/cm}^3$ ), while the QMD and DFT-AA models were performed at  $2.05 \text{ g/cm}^3$ . However, the thermal conductivities from Purgatorio at  $1.84$  and  $2.05 \text{ g/cm}^3$  are nearly the same, which suggests that the effect of the small density variation is negligible.

The values for the thermal conductivity in the Purgatorio code<sup>11,12</sup> depend strongly on the choice of structure factor used in the extended Ziman formulation<sup>19</sup>. The range of the Purgatorio prediction for Be with different structure factors is displayed as the pink shaded area in Fig. 6d, while the recommended value is plotted as the red curve. The recommended value is based on the inelastic scattering component as described in refs. 20,21. The maximum thermal conductivity value is given by the Debye–Hückel model<sup>22</sup>, which has been shown to give a minimum bound for the structure factor, and hence a maximum for the conductivity<sup>23</sup>. In this work, the structure factor responsible for the minimum conductivity at lower temperatures is the one-component plasma (OCP) model<sup>24</sup>. Above  $2.5 \text{ eV}$ , the model in





**Fig. 7** Effect of radiation transport and ballistic transport. **a**  $L_{CH}$  vs time. **b**  $L_{Be}$  vs time. Rad off radiation is turned off. Rad on radiation is included. Flxe 0.01-0.4: the electron flux limiter is varied from 0.01 to 0.4. Conde 0: electron thermal conduction is turned off. Conde 3x: electron thermal conduction is multiplied by 3 ×. Numerical: the numerical solution of the conduction equations as described in the text. The numerical results agree with the HYADES simulations.

ref. <sup>20</sup> retaining the elastic term provided a lower thermal conductivity than the OCP. Note that these minimum values are limited primarily by the available structure factor models implemented in the Purgatorio code; while they are chosen to provide a representative sampling of possible structure factors, they are not guaranteed to provide a rigorous lower bound on the thermal conductivity. Additional details on the selection of structure factors are provided in ref. <sup>25</sup>.

We find that the inferred CH thermal conductivity is in reasonable agreement with Purgatorio, QMD, and both the Spitzer and the LMD models with electron-electron collisions. Without this correction term, the predictions from Spitzer and LMD are too high for CH. For Be, the QMD prediction falls within the error range. The LMD and the DFT-AA predictions spanned by the solid and the dashed curves also overlap with our measurement, while the Spitzer prediction does not agree with the data. Model predictions with the electron-electron correction, including Spitzer + ee, LMD + ee, DFT-AA + ee, and Purgatorio (with the recommended structure factor), all appear to be lower than the value inferred from the data. The comparison indicates that the correction from electron-electron collisions has been overestimated for Be. Recent researches indicate that the current way of estimating this correction term has a lot of uncertainties<sup>26-28</sup>. On the other hand, the measured Be thermal conductivity falls within the range of the Purgatorio predictions using different structural factors, which suggests another possible explanation for the disagreement. In fact, the measured value is close to the upper bound of the Purgatorio prediction given by ref. <sup>22</sup>. Our results motivate further investigation into the electron-electron collision effect, the structure factor, as well as other aspects of thermal transport in a warm dense matter regime.

## Discussion

Besides thermal conduction, there are other processes that could affect the density scale lengths near the interface. We have thoroughly examined a list of these processes as discussed below, and confirmed that thermal conduction is the dominant process.

Hydro-instabilities at the interface could modify the scale lengths. The growth rate is  $\sigma_{RT} = \sqrt{A_t a k}$  for classical Rayleigh–Taylor instability and  $\sigma_{RM} = A_t k \Delta u$  for Richtmyer–Meshkov instability, where  $A_t$  is the Atwood number,  $A_t = (\rho_2 - \rho_1)/(\rho_2 + \rho_1)$ ,  $k$  is the wavenumber of the surface perturbation,  $a$  is the acceleration, and  $\Delta u$  is the velocity change. Because the motion of the interface is very little, as observed in the experiments, the growth rate of the instabilities is very small. The scanning electron microscopy (SEM) characterization of the surface shows  $k \sim 0.05 \mu\text{m}^{-1}$ . Given  $A_t = 0.34$  and an upper limit of the velocity  $1 \mu\text{m/ns}$ , the growth rates are estimated to be less than  $0.017 \text{ ns}^{-1}$ . The amplitude of the instabilities at 7 ns will be less than  $0.26 \mu\text{m}$ , much smaller than the measured scale lengths at 6.8 ns. This conclusion has been confirmed by 2D hydrodynamic simulations performed with the code HYDRA<sup>29</sup> which showed negligible instability growth at the interface.

Ballistic transport and radiation transport are also negligible under our experimental conditions. Figure 7 shows the time history of scale lengths in CH (a) and Be (b) from a series of 1D hydrodynamic simulations using HYADES<sup>30</sup> with radiation transport turned on/off and various electron flux limiters. The initial density profile was a step function between CH and Be. These simulations employ a built-in Lee–More model for thermal conductivity. The three curves for radiation on/off and electron flux limiters ranging from 0.01 to 0.4 are overlapped, showing that radiation and ballistic transport have a negligible effect on the evolution of the density scale lengths. Both  $L_{CH}$  and  $L_{Be}$  stay almost constant when the electron thermal conduction is turned off, and increase significantly over time when the electron thermal conduction is multiplied by 3 ×, indicating that electron thermal conduction is the dominant process here.

Hot electrons generated at the laser-plasma interaction (LPI) region could contribute to the heating of the interface. The laser intensity is  $2 \times 10^{15} \text{ W/cm}^2$  on the target in these experiments. Using the conversion efficiency in ref. <sup>31</sup>, we carried out LASNEX<sup>32</sup> simulations with three hot electron temperatures, 10, 60, and 200 keV. If  $T_{\text{hot}} = 10 \text{ keV}$ , hot electrons will not affect the interface as they are stopped inside the 500- $\mu\text{m}$ -thick Be foil. For

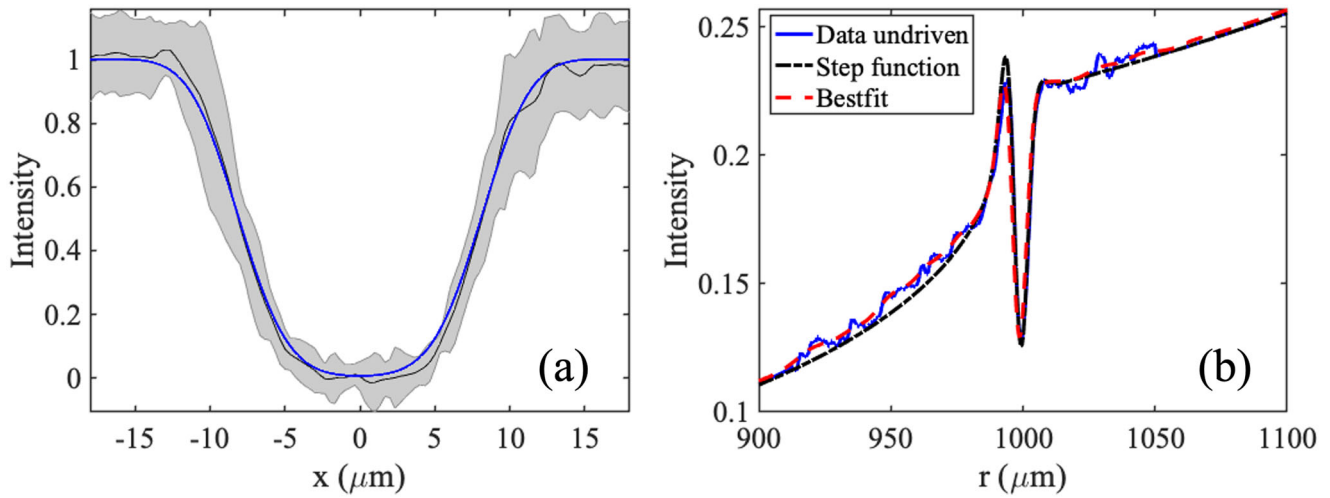


**Fig. 8 Instrument function of the system. a** Determine the system instrument function with Au grid radiographs. The black curve is an average intensity lineout from eight Au grid radiographs and the shaded areas are the error bars. The blue line is the best fit when we convolute the theoretical intensity with an instrument function. We found that the instrument function is a Gaussian with an FWHM of 6.1  $\mu\text{m}$ . **b** The blue curve is the measured RER lineout for an unheated target. The black dashed curve is the calculated intensity using an unperturbed step function as the density profile and a Gaussian with an FWHM of 6.1  $\mu\text{m}$  as the instrument function. The red dashed curve is the intensity calculated using the extracted undriven density profile shown in Fig. 3 that best fits the data.

more energetic electrons, the hot electron-induced heat is  $\sim 0.5\text{ eV}$  for  $T_{\text{hot}} = 60\text{ keV}$  and  $\sim 2\text{ eV}$  for  $T_{\text{hot}} = 200\text{ keV}$ . The lifetime of these hot electrons is only 10–20 ps, hence we do not expect them to play a role after a few ns when the measurements are made. Furthermore, the temperature near the interface is determined in situ using the local wave velocities, independent of the source of the heating. There could be photoelectrons generated by the 3 keV heating x-rays. Their stopping distance is less than 0.3  $\mu\text{m}$  therefore, this effect is negligible as well.

There can be an oxidation layer at the Be surface, modifying the local opacity and, thus, the temperature after the x-ray heating. The thickness of the oxidation layer is about 5 nm. We included this layer of BeO in HYADES runs, and the effect turned out to be negligible, mainly because the layer is so thin that the modification is limited to a spatial scale much less than the observed scale lengths.

It should be noted that ionic contributions are not included in the Pugatorio table. However, ionic conduction is expected to be much smaller than electronic conduction at a few eV temperatures. Thermal convection carried by collective particle motion at the atomic scale is not considered here. We hope that these results will motivate both experimental and theoretical efforts to improve our knowledge of the transport properties of warm dense matter.

**Methods**

**Instrument function.** The contrast of the refractive fringe is affected by three factors: x-ray source size or the instrument function of the imaging system, density at each side of the interface, and the density scale length near the interface. All these factors can be obtained in situ from the radiographs. The instrument function of the system can be determined by the Au grid shown in Fig. 2b. We have taken a total of 8 grid measurements. The average intensity lineout with error bars is shown in Fig. 8a. We can fit the average intensity when we convolute the theoretical intensity with a Gaussian function that has an FWHM of 6.1  $\mu\text{m}$ , which also suggests that the resolution of the system is around 6  $\mu\text{m}$ . This value is quite close to the  $\sim 5\text{ }\mu\text{m}$  slit size. The instrument function can further be confirmed with the unheated radiograph. An ideal interface is a step function with cold CH and Be densities. The RER lineout it generates with the Gaussian instrument function is the black dashed curve in Fig. 8b. It agrees with the measured blue curve reasonably well, but with some subtle differences, as the fringe peak of the black curve is higher than that of the blue curve. For a better fit, we have to have a smaller slope on the CH side. The density profile that best fits the data were shown in the top row of Fig. 3. It was extracted with the density retrieval method described in the next section (see Density retrieval). The corresponding intensity is shown as the red dashed curve in Fig. 8b, which agrees very well with the data. The interface can be fitted using a Fermi function with a small density scale length of 0.8  $\mu\text{m}$  on the CH

side, while keeping a sharp interface on the Be side. The targets were fabricated when we filled melted CH into precisely machined Be tubes and let it solidify, so we did expect an imperfect interface on the CH side.

**Density retrieval.** Extracting the density profile from the RER lineout appears to be similar to a phase retrieval problem, as the electron density profile directly determines the phase. Retrieving the phase information from one single intensity measurement is usually considered an ill-defined problem, as there could be an infinite number of amplitude and phase combinations at the object plane that can result in the same intensity at the image plane. However, our problem here is intrinsically different. At low temperatures, the real part ( $\delta$ ) and the imaginary part ( $\beta$ ) of the index of refraction for both CH and Be at regular electron density  $n_{e0}$  are known, and the index of refraction is linearly proportional to the electron density.  $\delta_{CH} + i\beta_{CH} = n_{e,CH}/n_{e0,CH}(\delta_{0,CH} + i\beta_{0,CH})$ ,  $\delta_{Be} + i\beta_{Be} = n_{e,Be}/n_{e0,Be}(\delta_{0,Be} + i\beta_{0,Be})$ . Therefore, the phase  $\phi$  at the object plane is proportional to the Abel transform of the electron density, specifically we have

$$\phi(x) = \begin{cases} \frac{2k\delta_{0,CH}}{n_{e0,CH}} \int_x^{r_0} \frac{n_e(r)r}{\sqrt{r^2-x^2}} dr \\ + \frac{2k\delta_{0,Be}}{n_{e0,Be}} \int_{r_0}^R \frac{n_e(r)r}{\sqrt{r^2-x^2}} dr, & \text{if } x < r_0 \\ \frac{2k\delta_{0,Be}}{n_{e0,Be}} \int_x^R \frac{n_e(r)r}{\sqrt{r^2-x^2}} dr, & \text{if } x \geq r_0 \end{cases} \quad (3)$$

Here  $r_0$  is the radius of the CH/Be interface,  $R$  is the outer radius of the target cylinder, and  $k$  is the wavenumber of the backscatterer X-ray. Similarly, the amplitude change at the object plane can be written as

$$A(x) = \begin{cases} \exp\left(-\frac{2k\beta_{0,CH}}{n_{e0,CH}} \int_x^{r_0} \frac{n_e(r)r}{\sqrt{r^2-x^2}} dr\right) \\ - \frac{2k\beta_{0,Be}}{n_{e0,Be}} \int_{r_0}^R \frac{n_e(r)r}{\sqrt{r^2-x^2}} dr, & \text{if } x < r_0 \\ \exp\left(-\frac{2k\beta_{0,Be}}{n_{e0,Be}} \int_x^R \frac{n_e(r)r}{\sqrt{r^2-x^2}} dr\right), & \text{if } x \geq r_0 \end{cases} \quad (4)$$

Or we can write the amplitude as

$$A(x) = \begin{cases} \exp\left\{-\frac{\beta_{0,CH}}{\delta_{0,CH}} [\phi(x) - \phi(r_0)] - \frac{\beta_{0,Be}}{\delta_{0,Be}} \phi(r_0)\right\}, & \text{if } x < r_0 \\ \exp\left(-\frac{\beta_{0,Be}}{\delta_{0,Be}} \phi(x)\right), & \text{if } x \geq r_0 \end{cases} \quad (5)$$

Unlike traditional phase retrieval problems, in our case, there can only be one amplitude corresponding to a certain phase lineout. We cannot have arbitrary (phase, amplitude) combinations at the object plane. Another obvious constraint in our problem is the boundary condition. Both CH and Be that are further away (say  $>100\text{ }\mu\text{m}$ ) from the interface would stay intact, which sets fixed values for the retrieved electron density profile.

With traditional phase retrieval algorithms<sup>33,34</sup>, it is very difficult to implement the physics constraints; therefore, they tend to produce unphysical density profiles. Recently, deep learning has shown great potential for solving phase imaging problems, but most work requires a large amount of labeled experimental and synthetic data to train the neural network<sup>35</sup>. Wang et al.<sup>36</sup> has demonstrated a method to recover phase using a neural network combined with a Fresnel

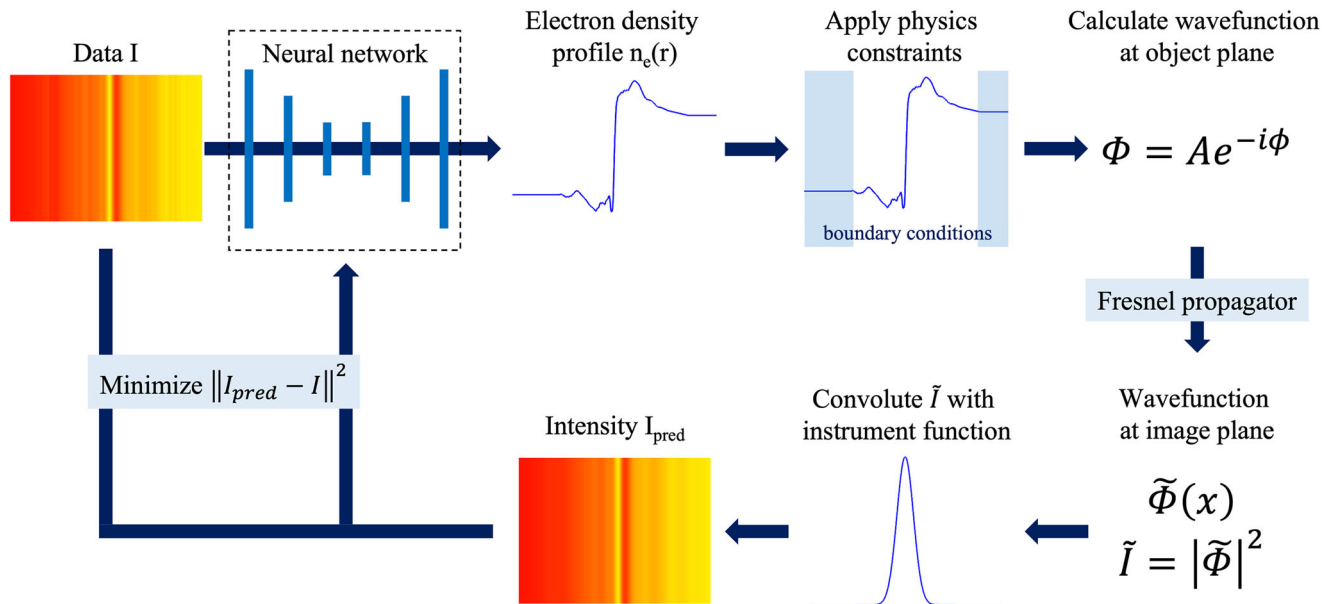


**Fig. 9 Density retrieval algorithm.** Schematic diagram showing the procedures to retrieve electron density profile from measured intensity lineout.

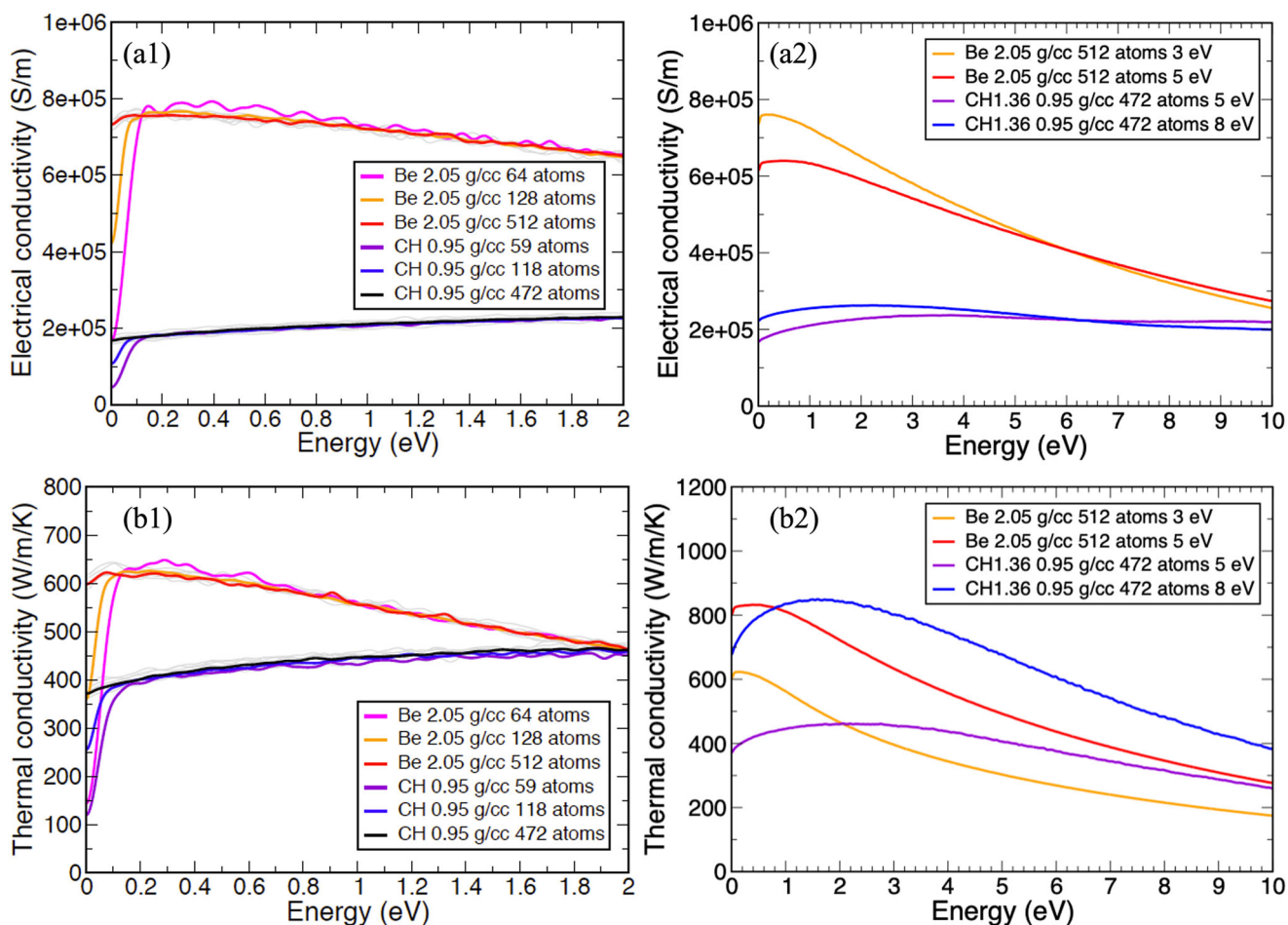


**Fig. 10 Electrical and thermal conductivities from quantum molecular dynamics (QMD) calculations.** **a1, a2** Electrical conductivities of Be and CH from QMD/KG. **b1, b2** Thermal conductivities of Be and CH from QMD/KG. Here **(a1)** and **(b1)** were calculated for Be at a temperature of 3 eV and CH at a temperature of 5 eV. Various system sizes were used to check the convergence. Electrical and thermal conductivities for Be and CH at two different temperatures are shown in **(a2), (b2)**.

propagator. We have adopted a similar method, but the electron density profile came out as a direct prediction of the neural network so that we could calculate both the phase and the amplitude directly from the electron density, and apply physics constraints inside our optimization routine. The process is illustrated in Fig. 9. Similar to ref. 36, a conventional artificial network U-Net<sup>37</sup> was used (we have modified it to 1D to accommodate our problem), but this network does not need to be trained beforehand. A single measured RER lineout is the only input and the predicted electron density profile would be the output. We can then, in general, apply any physics constraints to the predicted density profile, and in this particular problem, we set the boundary conditions. The amplitude and phase at the object plane are calculated according to Equations (3) and (4), and the wavefunction is just  $\Phi(x) = A(x)\exp^{-i\phi(x)}$ . The wavefunction is then propagated to the image plane with the Fresnel propagator

$$\begin{aligned}\tilde{\Phi}(x) &= \int \Phi(\xi)h(x-\xi)d\xi \\ h(x) &= \frac{z}{i\lambda} \frac{\exp(ik\sqrt{z^2+x^2})}{z^2+x^2}\end{aligned}\quad (6)$$

where  $z$  is the effective propagation distance determined by  $z_d z_s / (z_d + z_s)$ . Here  $z_s$  is the distance between the target and the source, and  $z_d$  is the distance between the target and the detector.  $\lambda$  is the X-ray wavelength. We can calculate the predicted intensity at the image plane as  $|\tilde{\Phi}|^2$ , and convolute it with the instrument function that we have predetermined using the Au bar data to get the predicted intensity lineout  $I_{\text{pred}}$ .  $I_{\text{pred}}$  can now be directly compared to the experimental data  $I$ , and we train the neural network to minimize the difference between  $I_{\text{pred}}$  and  $I$ . The electron density profile  $n_e = \text{argmin}_{n_e} \|I_{\text{pred}} - I\|^2$ .

**DFT-MD simulations.** Our DFT-MD simulations were carried out with the Vienna ab initio Simulation Package (VASP)<sup>38–41</sup>. We performed Born–Oppenheimer MD within the  $NVT$  ensemble with a Langevin thermostat<sup>42</sup> with a friction coefficient of  $10 \text{ ps}^{-1}$ . The generalized gradient approximation (GGA) of DFT with the Perdew–Burke–Ernzerhof (PBE) exchange–correlation functional<sup>43,44</sup> and the associated projector-augmented wave (PAW) pseudopotentials<sup>45,46</sup> were used. The electronic density was constructed from a single-particle wavefunction sampled at the  $(1/4, 1/4, 1/4)$  point of the Brillouin zone. The Mermin formulation of DFT is used where the Kohn–Sham single-particle states are occupied according to a Fermi–Dirac distribution at the chosen average ionic temperature<sup>47</sup>. For beryllium, we ran simulations at a density of  $2.05 \text{ g/cm}^3$ , a temperature of 3 and 5 eV with three system sizes (64, 128, and 512 atoms) in order to explore the impact of system size on the DC limit of the electrical and thermal conductivities. For the plastic, we used a stoichiometry of  $\text{C}_1\text{H}_{1.36}$ , a density of  $0.95 \text{ g/cm}^3$ , a temperature of 5 and 8 eV, and three system sizes (59, 118, and 472 atoms). The simulations were run for 5 ps after equilibration. For the small and medium-size calculations, 200 well-spaced configurations were used for the conductivity calculations, while 100 were used for the larger calculations. For the larger simulations, the molecular dynamics was accelerated using the machine-learned force field in VASP 6.3<sup>48–50</sup>.

To calculate optical and transport properties, the Onsager coefficients  $L_{mn}$  were computed according to the Kubo–Greenwood formulation<sup>51–53</sup>.

$$\begin{aligned}L_{mn}(\omega) &= (-1)^{m+n} \frac{2\pi e^{4-m-n}}{3Vm_e^2\omega} \\ &\times \sum_{i,j,\alpha,k} \left( \frac{\epsilon_{i,k} + \epsilon_{j,k}}{2} - h_e \right)^{m+n-2} \\ &\times |\langle \psi_{i,k} | p_\alpha | \psi_{j,k} \rangle|^2 \\ &\times [f(\epsilon_{i,k}) - f(\epsilon_{j,k})] \delta(\epsilon_{j,k} - \epsilon_{i,k} - \hbar\omega),\end{aligned}\quad (7)$$

where  $m, n = 1, 2$ .  $i$  and  $j$  are band labels.  $\alpha, k$  denotes the Cartesian directions and  $k$  points.  $e, m_e, V, \omega$ , and  $h_e$  are the electronic charge, mass, cell volume, frequency and enthalpy per electron, respectively.  $\psi_{i,k}$  and  $\epsilon_{i,k}$  are the electronic eigenstates and eigenvalues of the electronic band  $i$  at a given  $k$  point.  $f(\epsilon_{i,k})$  is the Fermi distribution function. Here, the sum is over all  $k$ -points within the Brillouin zone, all bands included in the calculation, and the three Cartesian coordinates. The parameter  $L_{11}$  equals the real component of the frequency-dependent electrical conductivity ( $\sigma$ ), i.e.  $\sigma(\omega) = L_{11}(\omega)$ . The thermal conductivity  $K$  is defined as:

$$K(\omega) = \frac{1}{T} \left( L_{22}(\omega) - \frac{L_{12}(\omega)L_{21}(\omega)}{L_{11}(\omega)} \right).\quad (8)$$

and the ratio of thermal and electrical conductivities divided by temperature is known as the Lorenz number:

$$L = \frac{e^2}{k_B^2 T} \frac{K}{\sigma}\quad (9)$$

which is constant (and equal to  $\pi^2/3$ ) in the limit of high density according to the Wiedemann–Franz law.

Figure 10a1, b1 shows the frequency dependence of the conductivities for Be and CH as a function of the number of atoms used in the QMD simulations. For these disordered systems, the larger the simulation, the smaller the excitation energies that can be calculated and the closer we can get to the DC limit. Similar

trends have been seen in warm dense hydrogen<sup>54</sup> and iron<sup>55</sup>. We get the DC limit of the electrical and thermal conductivities by extrapolating to 0 frequency, as is shown in Fig. 10a2, b2. Given the larger simulations that were performed, we have a very good estimate the DC limit.

## Data availability

The data that support the findings of this study are available from the corresponding author upon reasonable request.

Received: 14 July 2022; Accepted: 31 March 2023;

Published online: 10 May 2023

## References

- DOE office of Science and NNSA. *Report of the Workshop on High Energy Density Laboratory Physics Research Needs, Basic Research Needs for High Energy Density Laboratory Physics*. [https://science.osti.gov/-/media/fes/pdf/workshop-reports/Hedlp\\_brn\\_workshop\\_report\\_oct\\_2010.pdf](https://science.osti.gov/-/media/fes/pdf/workshop-reports/Hedlp_brn_workshop_report_oct_2010.pdf) (2009).
- Hammel, B. A. et al. High-mode Rayleigh–Taylor growth in NIF ignition capsules. *High Energy Density Phys.* **6**, 171 (2010).
- Ping, Y. et al. Differential heating: a versatile method for thermal conductivity measurements in high-energy-density matter. *Phys. Plasmas* **22**, 092701 (2015).
- Ping, Y. et al. Refraction-enhanced x-ray radiography for density profile measurements at CH/Be interface. *JINST* **6**, P09004 (2011).
- Koch, J. A. et al. Refraction-enhanced x-ray radiography for inertial confinement fusion and laser-produced plasma applications. *J. Appl. Phys.* **105**, 113112 (2009).
- Henke, B. L., Gullikson, E. M. & Davis, J. C. X-ray interactions: photoabsorption, scattering, transmission, and reflection at  $E = 50\text{--}30,000 \text{ eV}$ ,  $Z = 1\text{--}92$ . *At. Data Nucl. Data Tables* **54**, 181 (1993).
- Dewald, E. L. et al. X-ray streaked refraction enhanced radiography for inferring inflight density gradients in ICF capsule implosions. *Rev. Sci. Instrum.* **89**, 10G108 (2018).
- More, R. M., Warren, K. H., Young, D. A. & Zimmerman, G. B. A new quotidian equation of state (QEOS) for hot dense matter. *Phys. Fluids* **31**, 3059 (1988).
- Young, D. A. & Corey, E. M. A new global equation of state model for hot, dense matter. *J. Appl. Phys.* **78**, 3748 (1995).
- Wu, C. J. et al. Development of a multiphase Beryllium equation of state and physics-based variations. *J. Phys. Chem. A* **125**, 1610 (2021).
- Wilson, B., Sonnad, V., Sterne, P. & Isaacs, W. PURGATORIO—a new implementation of the INFERNO algorithm. *J. Quant. Spectrosc. Radiat. Transf.* **99**, 658 (2006).
- Sterne, P. A., Hansen, S. B., Wilson, B. G. & Isaacs, W. A. Equation of state, occupation probabilities and conductivities in the average atom Purgatorio code. *High Energy Density Phys.* **3**, 278 (2007).
- Spitzer Jr, L. & Härm, R. Transport phenomena in a completely ionized gas. *Phys. Rev.* **89**, 977 (1953).
- Lee, Y. T. & More, R. M. An electron conductivity model for dense plasmas. *Phys. Fluids* **27**, 1273 (1984).
- Desjarlais, M. P. Practical improvements to the Lee–More conductivity near the metal–insulator transition. *Contrib. Plasma Phys.* **41**, 267 (2001).
- Callow, T. J., Hansen, S. B., Kraissler, E. & Cangi, A. First-principles derivation and properties of density-functional average-atom models. *Phys. Rev. Res.* **4**, 023055 (2022).
- Hu, S. X. et al. First-principles investigations on ionization and thermal conductivity of polystyrene for inertial confinement fusion applications. *Phys. Plasmas* **23**, 042704 (2016).
- Atzeni, S. & Meyer-ter-Vehn, J. *The Physics of Inertial Fusion* (Clarendon Press, 2004).
- Evans, R., Gyorffy, B. L., Szabo, N. & Ziman, J. M. In *The Properties of Liquid Metals* (ed. Takeuchi, S.), pages 319–331 (Wiley, 1973).
- Baiko, D. A., Kaminker, A. D., Potekhin, A. Y. & Yakovlev, D. G. Ion structure factors and electron transport in dense Coulomb plasmas. *Phys. Rev. Lett.* **81**, 5556 (1998).
- Potekhin, A. Y., Baiko, D. A., Haensel, P. & Yakovlev, D. G. Transport properties of degenerate electrons in neutron star envelopes and white dwarf cores. *Astron. Astrophys.* **346**, 345 (1999).
- Debye, P. & Hückel, E. Zur Theorie der Elektrolyte. I. Gefrierpunkte, niedrige und verwandte Erscheinungen. *Z. Physik* **24**, 185 (1923).
- Mermin, N. D. Exact lower bounds for some equilibrium properties of a classical one-component plasma. *Phys. Rev.* **171**, 272 (1968).
- Young, D. A., Corey, E. M. & DeWitt, H. E. Analytic fit to the one-component-plasma structure factor. *Phys. Rev. A* **44**, 6508 (1991).

25. Hansen, S. B. et al. Electrical conductivity calculations from the Purgatorio code. In *Proc. NEDCP UCRL-PROC-218150* (Lawrence Livermore National Laboratory, 2005).
26. Shaffer, N. R. & Starrett, C. E. Model of electron transport in dense plasmas spanning temperature regimes. *Phys. Rev. E* **101**, 053204 (2020).
27. Kononov, A. et al. Electron dynamics in extended systems within real-time time-dependent density-functional theory. *MRS Comm.* **12**, 1002 (2022).
28. Kratzer, P. & Zahedifar, M. Relaxation of electrons in quantum-confined states in Pb/Si(111) thin films from master equation with first-principles-derived rates. *New J. Phys.* **21**, 123023 (2019).
29. Marinak, M. M. et al. Three-dimensional HYDRA simulations of National Ignition Facility targets. *Phys. Plasmas* **8**, 2275 (2001).
30. Larsen, J. T. & Lane, S. M. HYADES-A plasma hydrodynamics code for dense plasma studies. *J. Quant. Spectrosc. Radiat. Transf.* **51**, 179 (1994).
31. Vu, H. X., DuBois, D. F., Myatt, J. F. & Russell, D. A. Hot-electron generation by “cavitating” Langmuir turbulence in the nonlinear stage of the two-plasmon-decay instability. *Phys. Plasmas* **19**, 102703 (2012).
32. Zimmerman, G. B. & Kruer, W. L. Numerical simulation of laser-initiated fusion. *Comments Plasma Phys. Controlled Fusion* **2**, 51 (1975).
33. Schropp, A. et al. Imaging shock waves in diamond with both high temporal and spatial resolution at an XFEL. *Sci. Rep.* **5**, 11089 (2015).
34. Shechtman, Y. et al. Phase retrieval with application to optical imaging: a contemporary overview. *IEEE Signal Process. Mag.* **32**, 87 (2015).
35. Barbastathis, G., Ozcan, A. & Situ, G. On the use of deep learning for computational imaging. *Optica* **6**, 921 (2019).
36. Wang, F. et al. Phase imaging with an untrained neural network. *Light Sci. Appl.* **9**, 77 (2020).
37. Ronneberger, O., Fischer, P. & Brox, T. U-net: convolutional networks for biomedical image segmentation. In *Proc. 18th International Conference on Medical Image Computing and Computer-Assisted Intervention* 234–241 (Springer, 2015).
38. Kresse, G. & Hafner, J. Ab initio molecular dynamics for liquid metals. *Phys. Rev. B* **47**, 558(R) (1993).
39. Kresse, G. & Hafner, J. Ab initio molecular-dynamics simulation of the liquid-metal-amorphous-semiconductor transition in germanium. *Phys. Rev. B* **49**, 14251 (1994).
40. Kresse, G. & Furthmüller, J. Efficiency of ab-initio total energy calculations for metals and semiconductors using a plane-wave basis set. *Comput. Mat. Sci.* **6**, 15 (1996).
41. Kresse, G. & Furthmüller, J. Efficient iterative schemes for ab initio total-energy calculations using a plane-wave basis set. *Phys. Rev. B* **54**, 11169 (1996).
42. Allen, M. P. & Tildesley, D. J. *Computer Simulation of Liquids* (Oxford Univ. Press, 1991).
43. Perdew, J. P., Burke, K. & Ernzerhof, M. Generalized gradient approximation made simple. *Phys. Rev. Lett.* **77**, 3865 (1996).
44. Perdew, J. P., Burke, K. & Ernzerhof, M. Generalized gradient approximation made simple. *Phys. Rev. Lett.* **78**, 1396 (1997).
45. Blöchl, P. E. Projector augmented-wave method. *Phys. Rev. B* **50**, 17953 (1994).
46. Kresse, G. & Joubert, D. From ultrasoft pseudopotentials to the projector augmented-wave method. *Phys. Rev. B* **59**, 1758 (1999).
47. Mermin, N. D. Thermal properties of the inhomogeneous electron gas. *Phys. Rev.* **137**, A1441 (1965).
48. Jinnouchi, R., Lahnsteiner, J., Karsai, F., Kresse, G. & Bokdam, M. Phase transitions of hybrid perovskites simulated by machine-learning force fields trained on the fly with Bayesian inference. *Phys. Rev. Lett.* **122**, 225701 (2019).
49. Jinnouchi, R., Karsai, F. & Kresse, G. On-the-fly machine learning force field generation: application to melting points. *Phys. Rev. B* **100**, 014105 (2019).
50. Jinnouchi, R., Karsai, F., Verdi, C., Asahi, R. & Kresse, G. Descriptors representing two- and three-body atomic distributions and their effects on the accuracy of machine-learned inter-atomic potentials. *J. Chem. Phys.* **152**, 234102 (2020).
51. Holst, B., French, M. & Redmer, R. Electronic transport coefficients from ab initio simulations and application to dense liquid hydrogen. *Phys. Rev. B* **83**, 235120 (2011).
52. Knyazev, D. V. & Levashov, P. R. Ab initio calculation of transport and optical properties of aluminum: influence of simulation parameters. *Comput. Mater. Sci.* **79**, 817 (2013).
53. Recoules, V., Lambert, F., Decoster, A., Canaud, B. & Clérrouin, J. Ab initio determination of thermal conductivity of dense hydrogen plasmas. *Phys. Rev. Lett.* **102**, 075002 (2009).
54. Lambert, F., Recoules, V., Decoster, A., Clrouin, J. & Desjarlais, M. P. On the transport coefficients of hydrogen in the inertial confinement fusion regime. *Phys. Plasmas* **18**, 056306 (2011).
55. Alfé, D., Pozzo, M. & Desjarlais, M. P. Lattice electrical resistivity of magnetic bcc iron from first-principles calculations. *Phys. Rev. B* **85**, 024102 (2012).

## Acknowledgements

We thank the OMEGA team at LLE for laser operation and technical support. We also would like to thank R. Wallace and the team at General Atomics for target fabrication. Helpful discussions with L. Benedict, R. Shepherd, and J. Koch are appreciated. This work was performed under the auspices of US DOE by LLNL under contract number DEAC52-07NA27344. This material is based upon work supported by the US Department of Energy, Office of Science, Office of Fusion Energy Sciences Early Career Research Program. S.B.H. acknowledges support by Sandia National Laboratories Laboratory Directed Research and Development program under project 218456. Sandia National Laboratories is a multimission laboratory managed and operated by National Technology & Engineering Solutions of Sandia, LLC, a wholly-owned subsidiary of Honeywell International Inc., for the US Department of Energy’s National Nuclear Security Administration under contract DE-NA0003525. This paper describes objective technical results and analysis. Any subjective views or opinions that might be expressed in the paper do not necessarily represent the views of the US Department of Energy or the United States Government. S.X.H. and G.W.C. acknowledge the support by the US Department of Energy National Nuclear Security Administration under Award Number DE-NA0003856, the University of Rochester, and the New York State Energy Research and Development Authority. This document was prepared as an account of work sponsored by an agency of the United States government. Neither the United States government nor Lawrence Livermore National Security, LLC, nor any of their employees make any warranty, expressed or implied, or assumes any legal liability or responsibility for the accuracy, completeness, or usefulness of any information, apparatus, product, or process disclosed, or represents that its use would not infringe privately owned rights. Reference herein to any specific commercial product, process, or service by trade name, trademark, manufacturer, or otherwise does not necessarily constitute or imply its endorsement, recommendation, or favoring by the United States government or Lawrence Livermore National Security, LLC. The views and opinions of authors expressed herein do not necessarily state or reflect those of the United States government or Lawrence Livermore National Security, LLC, and shall not be used for advertising or product endorsement purposes.

## Author contributions

Y.P., O.L.L., and G.W.C. designed and performed the experimental measurements. S.J. and Y.P. performed the data analysis. S.J. implemented the neural network method. H.D.W., P.S., S.H., S.B.H., R. L., and S.X.H. performed the theoretical work of calculating thermal conductivities from various models. D.S.C. and R.L. performed hydrodynamic simulations. S.H. performed the DFT-MD simulations. S.J. and Y.P. wrote the manuscript. All authors contributed to the improvement of the manuscript.

## Competing interests

The authors declare no competing interests.

## Additional information

**Correspondence** and requests for materials should be addressed to S. Jiang.

**Peer review information** *Communications Physics* thanks Zhandos Moldabekov and Jean Clerouin for their contribution to the peer review of this work.

**Reprints and permission information** is available at <http://www.nature.com/reprints>

**Publisher’s note** Springer Nature remains neutral with regard to jurisdictional claims in published maps and institutional affiliations.



**Open Access** This article is licensed under a Creative Commons Attribution 4.0 International License, which permits use, sharing, adaptation, distribution and reproduction in any medium or format, as long as you give appropriate credit to the original author(s) and the source, provide a link to the Creative Commons license, and indicate if changes were made. The images or other third party material in this article are included in the article’s Creative Commons license, unless indicated otherwise in a credit line to the material. If material is not included in the article’s Creative Commons license and your intended use is not permitted by statutory regulation or exceeds the permitted use, you will need to obtain permission directly from the copyright holder. To view a copy of this license, visit <http://creativecommons.org/licenses/by/4.0/>.

© The Author(s) 2023